Performance of Direct-Drive Cryogenic Targets on OMEGA

Introduction

In the inertial confinement fusion (ICF) approach to fusion, a spherical shell filled with a deuterium–tritium (DT) mixture is compressed to reach a temperature of 10 to 12 keV in the lower-density central core region (hot spot) to initiate a burn wave through the higher-density colder main fuel surrounding the core.[1–3] The main fuel areal density (ρR) at that time must be large enough to burn a significant fraction of the fuel.[1,2] The peak areal density depends mainly on the fuel adiabat (defined as a ratio of the shell pressure to the Fermi-degenerate pressure at the shell density) and laser energy:[4]

$$(\rho R)_{max} = \frac{2.6}{\alpha^{0.54}} E_{MJ}^{1/3}. \tag{1}$$

To study the physics of low-adiabat, high-compression fuel assembly, a series of experiments with cryogenic D_2 and DT fuel was designed and performed on OMEGA.[5] Figure 113.16
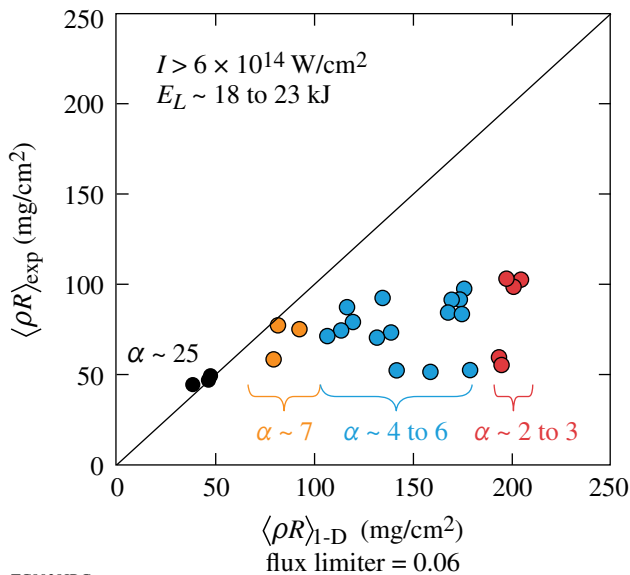

TC8038JRC

Figure 113.16
Measured neutron-averaged areal density $\langle \rho R \rangle$ as a function of the simulated value using the hydrocode *LILAC*, which uses a thermal conduction model with a constant flux limiter. The drive intensities were above 6×10^{14} W/cm² and the laser energy varied from 18 to 23 kJ.

summarizes the experimental results reported earlier.[6,7] The targets used in these experiments were D_2-filled CD shells with an outer diameter of ~860 μm, a shell thickness of 3 to 5 μm, and a cryogenic layer thickness between 92 and 98 μm. The targets were driven with shaped laser pulses at peak intensities of 6 to 10×10^{14} W/cm² to set the fuel adiabat at α = 2 to 25. Figure 113.16 compares the experimental areal density $\langle \rho R \rangle_{exp}$ inferred from the energy loss of the secondary protons[8] while they propagate through the compressed fuel and the simulated areal density $\langle \rho R \rangle_{1-D}$ averaged over the 1-D neutron-production history calculated using the hydrocode *LILAC*.[9] The constant flux-limiter thermal conduction model[10] with f = 0.06 was used in such simulations. As seen in the figure, the experimental data significantly deviate from simulation results for the implosions with a mid-to-low designed adiabat when the predicted $\langle \rho R \rangle_{1-D} > 100$ mg/cm². The goal of the current study presented here is to identify the main sources of the measured $\langle \rho R \rangle$ deviation from the theoretical predictions. Equation (1) is used for guidance in this study. According to this equation, the observed degradation in the areal density comes from the underestimation of the predicted adiabat.

In this article we consider several sources for the adiabat degradation during the implosion, including the shock heating and the preheat due to the suprathermal electrons. Based on the result of this study, target designs were optimized using the improved nonlocal thermal-conduction model implemented in the 1-D hydrodynamic code *LILAC*. High-areal-density[11] cryogenic fuel assembly with $\langle \rho R \rangle > 200$ mg/cm² has been achieved on OMEGA in designs where the shock timing was optimized and the suprathermal-electron preheat generated by the two-plasmon-decay instability was mitigated. The following sections (1) describe the modeling of the shock heating; (2) consider both the preheat effects due to the suprathermal electrons and the reduction in the measured areal density due to the burn truncation before the peak shell ρR is reached; and (3) present conclusions.

Modeling of Shock Heating

A typical laser pulse for a low-adiabat, direct-drive design consists of a lower-intensity foot (or, as shown in Fig. 113.17,

a picket used in adiabat-shaping designs[12,13] to mitigate the Rayleigh–Taylor instability growth[14]), a transition region, and the higher-intensity main pulse. At the beginning of the pulse, a shock wave (SW) is launched into the shell. Its strength determines the shell adiabat α. The compression wave (CW), initiated as the intensity rises during the transition region, must be properly timed to avoid an excessive adiabat increase at the inner part of the shell. Indeed, if the CW catches the SW too early in the shell, the SW strength increases, raising the adiabat. Delaying the CW, on the other hand, steepens up its front and turns into a shock as the CW travels along the density gradient produced by a rarefaction wave (RW) that is formed after the SW breaks out at the inner surface of the cryogenic layer. To prevent an excessive reduction in the fuel areal density, the coalescence of the RW with the CW must occur within the last 10% of the main fuel mass, as observed in calculations. This condition limits its allowable mistiming of the shock breakout to $\Delta t_s / t_s \leq 5\%$ and constrains the modeling accuracy in the absorbed laser energy E_s during the shock propagation. For a constant-intensity foot pulse, the shock-propagation time is $t_s = \Delta_0 / U_s$, where $U_s \sim \sqrt{P_a}$ is the shock speed and Δ_0 is the initial shell thickness. The ablation pressure scales as[1] $p_a \sim P^{2/3}$, where P is the laser power, and writing $E_s \sim P t_s$ gives $t_s \sim \Delta_0^{3/2} E_s^{-1/2}$. The same scaling can be obtained when the shock is launched by a narrow picket. The shock-breakout time in this case[12] is $t_s \sim \left(E_p^{-1/3} \Delta_0 \right)^\beta$, where $\beta = \left[1 - \sqrt{2\gamma(\gamma-2)} \big/ 2(2\gamma-1) \right]^{-1}$, γ is the ratio of specific heats, and t_p and E_p are the picket duration and energy, respectively. For $\gamma > 1.2$, the exponent is $\beta \simeq 3/2$ with less than 10% error, leading to $t_s \sim E_p^{-1/2}$, similar to the case of a constant-intensity pulse. Using $\Delta t_s / t_s < 5\%$, the requirement for the modeling accuracy in the absorbed picket energy becomes $\Delta E_p / E_p < 10\%$.

10.0

Power (TW)

1.0

Launch
compression
wave (CW)

0.1

Launch first shock wave (SW)

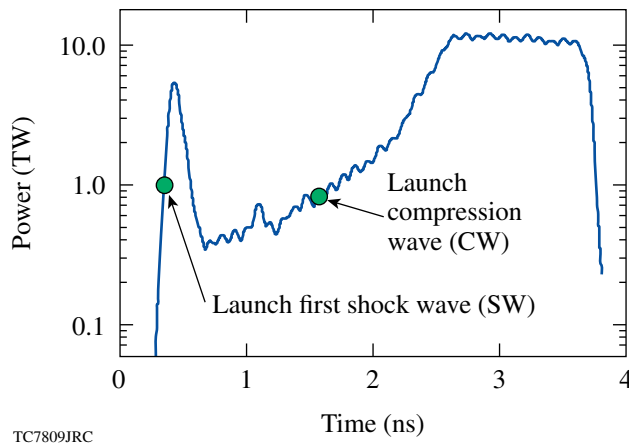0   1   2   3   4

Time (ns)

TC7809JRC

Figure 113.17
A typical pulse shape for the OMEGA direct-drive, low-adiabat design.

Inverse bremsstrahlung is the main absorption mechanism for the $\lambda = 0.351$-μm-wavelength laser irradiation. The absorption fraction depends on the electron-temperature and electron-density profiles.[15] These profiles, in turn, are determined by the thermal conduction near the location of the peak in the laser-energy deposition. Thermal-conduction modeling is crucial, therefore, when calculating the laser-energy deposition. In addition to inverse bremsstrahlung, resonance absorption[15] can be important at early times when the electron density at the critical surface is steep enough for the electric field to tunnel from the laser turning point to the critical density and excite plasma waves. The next two subsections study the contribution of resonance absorption and the effects of nonlocal electron transport to the laser absorption in ICF plasmas.

1. Resonance Absorption Modeling

The effect of resonance absorption was studied for direct-drive–relevant conditions using a numerical solution of the wave equations in planar geometry. The results of these calculations[16] were used to develop a simplified analytical model that can be implemented into hydrodynamic codes to model spherical implosions. The model is based on the approach described in Ref. 15. We consider a p-polarized electromagnetic wave with incident angle θ between the direction of propagation and the density gradient, which points along the z direction. The z component of the electric field E_z tunnels through from the laser turning point to the critical density, depositing a fraction f_A of the incident laser energy into the plasma waves (resonance absorption[15]). Propagating down the density gradient, the energy of these waves is damped into the electrons. Calculations show[16] that the average temperature of the resonance electrons for $\lambda_L = 0.351$-μm-wavelength laser irradiation does not exceed ~5 keV. Resonance absorption, therefore, enhances the local absorption due to the inverse bremsstrahlung. Resonance absorption is calculated by evaluating the energy flux[15] $I_{abs} = \int_0^\infty \nu E_z^2 \big/ 8\pi \, dz$, where ν is the damping rate of the plasma waves. The main contribution to this integral comes near the resonance point, in the vicinity of the critical density, resulting in

$$I_{abs} = \frac{\omega L_n}{8} \left(\sin\theta \, B_{cr} \right)^2, \qquad (2)$$

where B_{cr} and L_n are the magnetic field and the density scale length at the critical density, respectively. The resonance field is calculated by multiplying the field amplitude at the turning point, $B_t = 0.9 \, E_0 \left(c/\omega L_n \right)^{1/6}$, by a tunneling factor.[15] Here, E_0 is the laser field in free space. In deriving B_t the laser-energy absorption in the region below critical density was neglected, leading to an overestimate in the resonance field. Corrected

for this absorption and adding the intensity of the incoming and outgoing waves, $f_t E_0^2$ and $(f_t - f_A)E_0^2$, respectively, the magnetic field becomes $0.9\sqrt{2f_t - f_A} E_0 (c/\omega L)^{1/6}/2$, where f_t is the fraction of the laser energy that reaches the turning point. Multiplying B_t by the tunneling factor $\exp\left(-\omega/c \int_{z_t}^{z_c} \sqrt{-\epsilon} \, dz\right)$, we obtain $f_A = \phi^2 (2f_t - f_A)/8$ and

$$f_A = \frac{2f_t}{8/\phi^2 + 1}, \tag{3}$$

where $\phi = 2.3\tau \exp\left(-2\tau^3/3\right)$, $\tau = \left(3\omega/2c \int_{z_t}^{z_c} \sqrt{-\epsilon} \, dz\right)^{1/3}$, $\epsilon = 1 - n/n_{cr}$ is the dielectric function, n and n_{cr} are the electron and critical densities, respectively, and z_t and z_c are the position of the turning point and critical density, respectively. Since the incident laser light in ICF experiments consists of a mixture of s and p polarizations, the resonance absorption fraction in a hydrocode simulation is taken as a half value predicted by Eq. (3). Simulations show that Eq. (3) agrees very well with the results of more rigorous calculations.[16]

The tunneling factor depends on the density scale length at the critical surface. Thus, an accurate calculation of both the inverse bremsstrahlung and resonance absorption relies on thermal transport modeling, which affects hydrodynamic profiles in the energy-deposition region. The next subsection discusses electron thermal transport in laser-produced plasmas.

2. Heat-Transport Modeling

Because of the steep temperature and density profiles where the laser deposition is at maximum, the validity of Spitzer thermal conduction[17] breaks down (the mean free path of the heat-carrying electrons is comparable to or larger than the temperature scale length). In a model using flux limitation,[10] the thermal flux is calculated as a fraction f of the free-stream flux $q_{fs} = nT v_T$, when the Spitzer heat flux $q_{sp} > f q_{fs}$. Here, $v_T = \sqrt{T/m}$ is the electron thermal velocity and m, T, and n are the electron mass, temperature, and free electron density, respectively. Since the flux-limiter value f cannot be determined directly from the physical principles, its value, usually taken to be a constant in time, is obtained by comparing the simulation results with experimental observables. Remarkably, such a simple model is able to successfully explain a large number of experiments with simple pulse shapes. However, for the shaped, low-adiabat pulses, the flux limiter, as first shown in the Fokker–Planck simulations,[18] must be time dependent. The time dependence is especially important in simulating the adiabat-shaping designs,[12,13] where a narrow picket is introduced at the beginning of the laser pulse to tailor the shell adiabat and mitigate the

Rayleigh–Taylor instability growth.[14] Accurate accounting for the absorbed picket energy as well as for the laser coupling during the transition region (see Fig. 113.17) is crucial for the shock-timing calculation. Since it is highly impractical to obtain the temporal shape of the flux limiter based only on the experimental data, a thermal-transport model must be developed for self-consistent flux calculations. Such a model was proposed in Ref. 19, where the simplified Boltzmann equation was solved using the Krook approximation.[20] The main disadvantage of such a model is the lack of particle and energy conservation because of the energy-dependent collisional frequency. Calculations show that, for the conditions relevant to ICF experiments, the error in calculating the local electron density and energy using the solution of the model described in Ref. 19 does not exceed 5%. Despite the fact that the error is small, the model used in the present calculations is modified to recover the conservation properties. This is accomplished by renormalizing the local density and temperature used in evaluating the symmetric part of the electron-distribution function. Similar modifications appear in the classical limit when the ratio of the electron mean-free path λ_{ei} to the temperature scale length L_T is small.[21] The second-order deviations from the Maxwellian f_M, $f_{sym} = f_M + f_n + v^2 f_T$, where $f_{n,T} \sim O[(\lambda_{ei}/L_T)^2]$, are due in such a limit to the contribution from the electron–electron collisions.[21] These corrections are equivalent to the renormalization in the electron density and temperature used in the local Maxwellian distribution, $f_{sym} = f_M(n', T')$. Next, we describe the renormalization procedure used in the present nonlocal model.

The Boltzmann equation with the Krook collisional operator[20] $v_x \partial_x f + (eE_x/m) \partial_v f = -\nu_{ei}(v)(f - f_0)$ can be solved analytically by substituting f_0 into the second term of the left-hand side:[19]

$$f = f_0 - \int^x G(x',v) e^{\xi/y} \, d\xi,$$
$$G = \lambda_{ei}(x') \left(\frac{\partial f_0}{\partial x} + \frac{eE_x}{T} \frac{\partial f_0}{\partial \epsilon}\right), \tag{4}$$

where

$$\xi(x') = \int_x^{x'} dx'' / \lambda_{ei}(x''),$$

$\epsilon = mv^2/2T$, $y = \cos\theta$, $\lambda_{ei} = v/\nu_{ei}$, $\nu_{ei} \sim v^{-3}$ is the electron–ion collisional frequency, and E_x is the slowly varying electric field. Assuming that f_0 is a function of the renormalized density n' and temperature T', the relations between (n', T') and (n,T) are found by integrating Eq. (4), multiplied by 1 and $mv^2/2$, yielding $n = n' - R_1$ and $3nT/2 = 3n'T'/2 - R_2$, respectively, where

$$R_1 = 2\pi \int_0^\infty dv v^2 \int_0^1 dy (H_L - H_R),$$

$$R_2 = \pi m \int_0^\infty dv v^4 \int_0^1 dy (H_L - H_R),$$

$$H_L = \int_{x_L}^x G e^{\xi/y} d\xi,$$

and

$$H_R = \int_x^{x_R} G e^{-\xi/y} d\xi.$$

The integration limits are defined as

$$\int_x^{\{x_R, x_L\}} dx'' / \lambda_{ei} = \{+, -\}\infty.$$

The electric current and the heat flux are calculated using the standard definitions $j_x = e \int d^3 v v_x f$ and $q_x = m \int d^3 v v^2 v_x f / 2$. The electric field E_x is defined by the zero-current condition $j_x = 0$. This condition yields an integral equation for E_x, which is solved by the iteration method.[19] For the distribution function f_0, we use the Maxwellian function with the corrections due to the laser field[22] $f_0 = f_M \exp(-0.07 \alpha_L \epsilon^{5/2})$, where $\alpha_L = Z v_e^2 / v_T^2$, Z is the average ion charge, and v_e and $v_T = \sqrt{T/m}$ are the electron quiver and thermal velocities, respectively.

Two main effects are introduced by the nonlocal treatment of the thermal transport: First, the flux is reduced from the Spitzer value in the regions with steep temperature gradients; second, the main fuel is heated by the long-range electrons from the hotter plasma corona. The heat flux calculated using the distribution function in Eq. (4) does not correctly reproduce the nonlocal heating because the integrand in Eq. (4) does not go to zero at $\int_{x'}^x dx'' / \lambda_E = 1$, where λ_E is the electron-deposition range. Since the calculations must accurately account for every preheat source, it is essential to include a deposition cutoff. In the previous version of the nonlocal model,[19] this was accomplished by replacing the exponential kernel $e^{\xi/y}$ in Eq. (4) with $\sqrt{1 - \xi/y}$. Such a substitution, however, does not properly recover the Spitzer limit. In the current version of the model, a test-particle approximation is used in evaluating λ_{ei} to produce the deposition cutoff. This approach gives Spitzer conductivity when $\lambda_{ei}/L_T \ll 1$. In the test-particle approximation, λ_{ei} is calculated along the particle trajectory using the energy-loss equation $dK/ds = -K/2 \lambda_E$. Since $\lambda_E \sim K^2$, we obtain

$$K = K_0 \sqrt{1 - \int_{x'}^x dx'' / y \lambda_E},$$

where $ds = dx/y$ is a path element. Then, the deposition cutoff is introduced in Eq. (4) by replacing $\lambda_{ei}(x')$ with

$$\lambda_{ei}(x', x) = \lambda_{ei}(x')\left(1 - \int_{x'}^x dx' / y \lambda_E\right).$$

Next, we compare the results obtained using the described nonlocal model with simulations based on the flux-limited Spitzer conduction. Figure 113.18 shows the effective flux limiter (defined as a maximum ratio of the nonlocal heat flux to the free-stream flux q_{fs} in the vicinity of maximum q_{sp} in the plasma corona) as a function of time for an $\alpha = 2$ cryogenic implosion. The higher value of the flux limiter during the picket indicates a larger predicted laser absorption and a stronger SW, relative to calculations based on the constant flux-limiter model. Then, as the laser intensity relaxes after the picket, the effective flux limiter takes on a reduced value, leading to a weaker CW. If these effects are not properly modeled in a simulation, they lead to a significant shock mistiming and areal-density reduction.
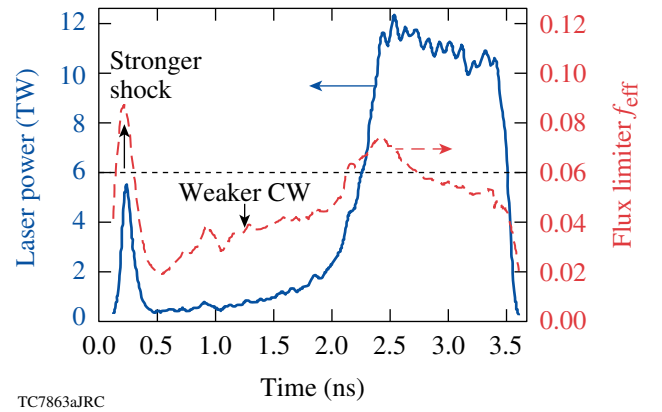

TC7863aJRC

Figure 113.18
Laser pulse (solid line, left axis) and the effective flux limiter f_{eff} (dashed line, right axis) obtained using the nonlocal model for an $\alpha = 2$ cryogenic OMEGA design with a 95-μm-thick D_2 layer and a 10-μm-thick CD overcoat. The thin dashed line shows standard values of the flux limiter used in the hydrocode *LILAC*.

To test the accuracy of the absorption calculations with the nonlocal transport model, the simulation results were compared with experimental absorption data[23] for implosions of 20-μm-thick plastic shells driven with a 200-ps Gaussian pulse at peak intensities varied from 5×10^{13} to 1.5×10^{15} W/cm^2. Figure 113.19 shows the laser absorption fraction calculated using the flux-limited transport model with $f = 0.06$ and no resonance absorption (open squares), the flux-limited model with resonance absorption (solid squares), and the nonlocal model with resonance absorption (triangles). The resonance absorption
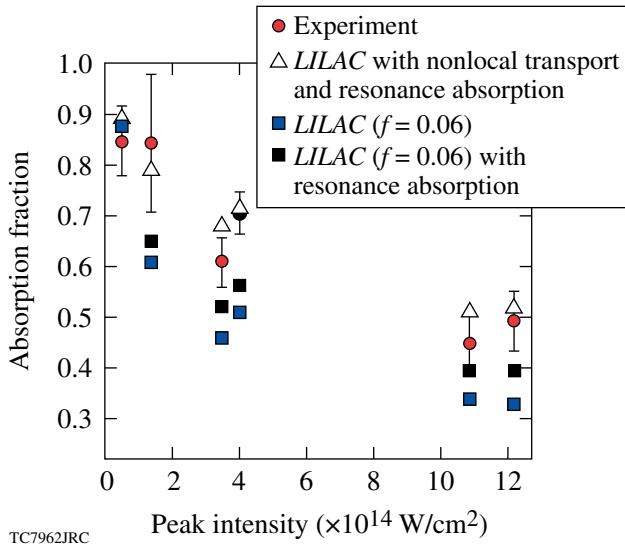
Figure 113.19
Absorption fraction of the incident laser energy for a 20-μm-thick CH shell driven by a 200-ps Gaussian pulse at different peak intensities.
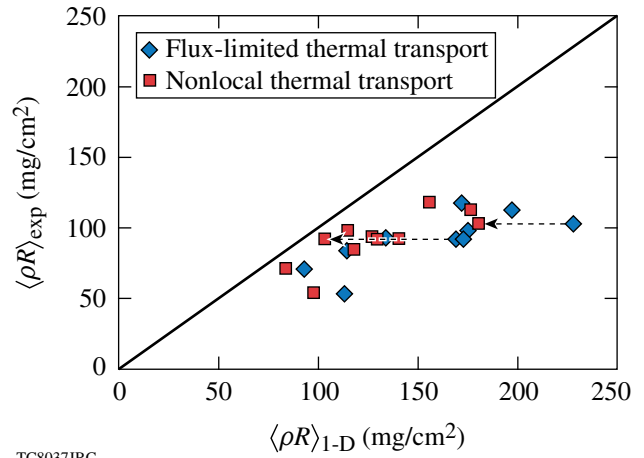
TC7962JRC

Figure 113.20
Measured $\langle \rho R \rangle$ in a thin CD cryogenic shell as a function of the simulated value using the hydrocode *LILAC* with a constant flux limiter $f = 0.06$ (diamonds) and the nonlocal (squares) thermal conduction models. Arrows indicate reduction in calculated $\langle \rho R \rangle$ when the nonlocal model is used.

TC8037JRC

effects are small when the nonlocal thermal-transport model is used. These results, therefore, are not shown in Fig. 113.19. The flux-limited transport model produces much steeper electron-density profiles near the laser turning point, resulting in larger resonance absorption in comparison with the nonlocal model calculations. However, even with resonance absorption taken into account, the flux-limited model underestimates the laser absorption fraction for most of the cases shown in Fig. 113.19. The nonlocal model, on the other hand, reproduces the experimental results very well. The non-monotonic behavior of the absorption fraction with peak intensity is due to shot-to-shot variations in the picket width and the rate of intensity rise.

Next, the areal densities for the cryogenic implosions shown in Fig. 113.16 were recalculated using the nonlocal thermal-transport model. The data are plotted in Fig. 113.20. The improved agreement with the experimental data is due to a reduction in the calculated areal density, resulting from significant shock mistiming predicted by the nonlocal model (see arrows in Fig. 113.20 showing this reduction for individual shots). Even though the calculations with the nonlocal model are in better agreement with the experimental data, some discrepancy still remains. In the next section we examine possible sources for the remaining discrepancy, starting with suprathermal-electron preheat.

Suprathermal-Electron Preheat and ρR Sampling

Several laser–plasma interaction processes are capable of generating suprathermal electrons in the plasma corona. As dis-

cussed in the **Introduction** (p. 16), the degradation in ρR is significant if the adiabat at the inner part of the shell is increased. The electron preheat is important, therefore, if the electron-deposition ranges exceed the thickness of the cold part of the shell during the implosion. Thus, for the OMEGA designs, only electrons with energy in excess of 50 keV can reduce the peak shell compression. To estimate the amount of the energy deposited in the shell required to degrade the fuel areal density, we use the pressure–density relation[1] $p \sim \alpha \rho^{5/3}$ and assume the ideal gas equation of state. This gives $\alpha \sim T^{5/3} / p^{2/3}$. The shell pressure is proportional to the ablation pressure p_a, which is determined by the laser intensity. Therefore, for a given drive intensity, according to Eq. (1), $\rho R = (\rho R)_0 / (T/T_0)^{0.09}$, where $(\rho R)_0$ and T_0 are the areal density and electron temperature without the effects of preheat. The shell temperature during the acceleration phase in a typical low-adiabat design is ~20 eV. A 20% reduction in the areal density corresponds to a 6-eV increase in the shell temperature. For an OMEGA target, this leads to ~10 J of preheat energy deposited into the unablated part of the shell. The lowest-threshold mechanism capable of producing energetic electrons with $T_{hot} > 50$ keV is the two-plasmon-decay instability.[15] The threshold parameter η for this instability[24] is

$$\eta = \frac{I_{14} L_n (\mu m)}{230\, T_{keV}} \frac{\lambda_L}{0.351\, \mu m}, \tag{5}$$

where I_{14} is the laser intensity in units of 10^{14} W/cm², L_n is the density scale length, and λ_L is the laser wavelength. The instability develops when $\eta > 1$. For a typical OMEGA implosion, $L_n \sim$

150 μm and $T_{keV} \sim 1$ at $I_{14} \sim 1$. Thus, the instability is expected to develop when the drive intensity exceeds a few 10^{14} W/cm^2.

The experimental signature of the suprathermal-electron preheat is the measured hard x-ray[25] signal. This correlates with the $3/2\omega$ signal,[23] indicating that the two-plasmon-decay instability is the main mechanism producing the energetic electrons. The hard x-ray signal measured in cryogenic implosions, shown in Fig. 113.21, increases with the laser intensity.[26] Taking this result into account, the peak drive intensity was reduced to below 3×10^{14} W/cm^2 to minimize the suprathermal-electron-preheat effect on the target performance.[26] The measured and predicted areal densities, together with the data for $I > 5 \times 10^{14}$ W/cm^2, are plotted on Fig. 113.22. The improved agreement observed for the lower-intensity shots suggests that suprathermal-electron preheat contributes to a modest degradation in ρR at higher drive intensities.

As the next step, the peak drive intensity was raised to 5×10^{14} and the CD overcoat thickness was increased from 5 to 10 μm. The thicker plastic shell was used to prevent the laser from burning through the plastic to the deuterium during the target implosion and thus mitigate the suprathermal-electron preheat at higher intensity. If the higher-Z plastic burns through during the pulse, as in the case of a 5-μm-thick shell, lower-Z D$_2$ penetrates into the subcritical-density region, reducing the laser absorption. This in turn leads to a drop in the coronal temperature and an increase in the laser intensity at the quarter-critical surface. All of these factors raise the value of η, exciting the two-plasmon-decay instability at the time when

Figure 113.22
Measured $\langle \rho R \rangle$ as a function of the simulated value using the hydrocode *LILAC* with the nonlocal transport model for cryogenic implosions at peak intensities $I > 5 \times 10^{14}$ W/cm^2 (squares) and $I < 3 \times 10^{14}$ W/cm^2 (circles), and for a 10-μm-thick CD shell at $I = 5 \times 10^{14}$ W/cm^2 (stars).

the CD layer burns through. Increasing the CD overcoat thickness to 10 μm allowed the drive intensity to be raised to 5×10^{14} W/cm^2. This produced a significantly less amount of the hard x-ray signal compared to the thinner plastic shell, indicating lower suprathermal preheat. The stars in Fig. 113.22 show the high areal densities (up to 202 ± 7 mg/cm^2) measured in the implosions, which are described in greater detail in Ref. 11. Despite the small hard x-ray signal, the measured areal densities were ~18% lower than the 1-D prediction, indicating that additional mechanisms could be responsible for the measured ρR deviation from the predicted value.

The areal density in the experiment is inferred from the energy downshift in the secondary protons created in the D^{3}He reaction.[8] The experimentally inferred $\langle \rho R \rangle$, therefore, is affected by the timing of the production of these protons with respect to the ρR temporal evolution. Shown in Fig. 113.23(a) are the experimental and predicted neutron-production histories for a cryogenic implosion with a 10-μm-thick CD overcoat that yielded the highest $\langle \rho R \rangle_{exp}$. The predicted areal-density history is plotted on the same figure. The figure shows that the experimental burn rate is significantly reduced (presumably by the perturbation growth during the shell deceleration) at the time when the shell ρR reaches its peak value.[27] This could explain the lower measured areal density with respect to the results of 1-D calculations [compare solid (measurement) and dotted (calculation) curves in Fig. 113.23(a)]. To address the
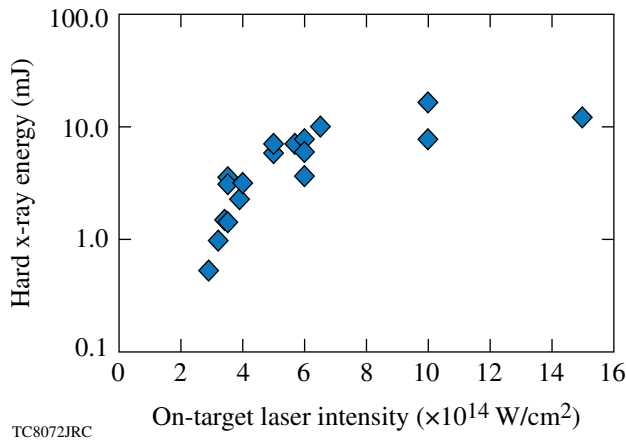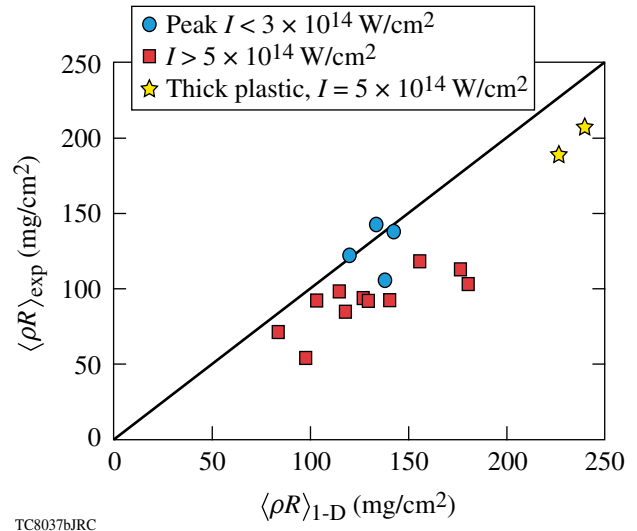

Figure 113.21
Measured bremsstrahlung radiation above 40 keV for the thin-CD-shell cryogenic implosions. The inferred hard x-ray temperature in these implosions is above 50 keV.

sampling issue, Fig. 113.23(b) plots the predicted D^3He proton spectrum averaged over the experimental burn history (dashed curve), showing good agreement with the measured spectrum (solid curve) averaged over five individual measurements at different views of the implosion.

The suprathermal-electron–generation efficiency for the NIF-scaled targets, not fully understood at present time, is currently under investigation. Preliminary experiments have been carried out to study the preheat mitigation by doping the outer layer of the ablator with high-Z elements. In these experiments, warm plastic shells filled with 15 atm of D_2 gas were imploded using two pulse shapes to set the shell adiabat to $\alpha = 2$ and 3, respectively. The outer 3 μm to 10 μm of the shell were doped with 6%/atom of Si or 2% to 2.6%/atom of Ge. The total shell thickness was 27 μm. The increased laser absorption caused by the higher averaged ion charge in the plasma corona is predicted to raise the threshold for the two-plasmon-decay instability [see Eq. (5)], reducing the suprathermal-electron preheat. Figure 113.24 shows the hard x-ray signal measured
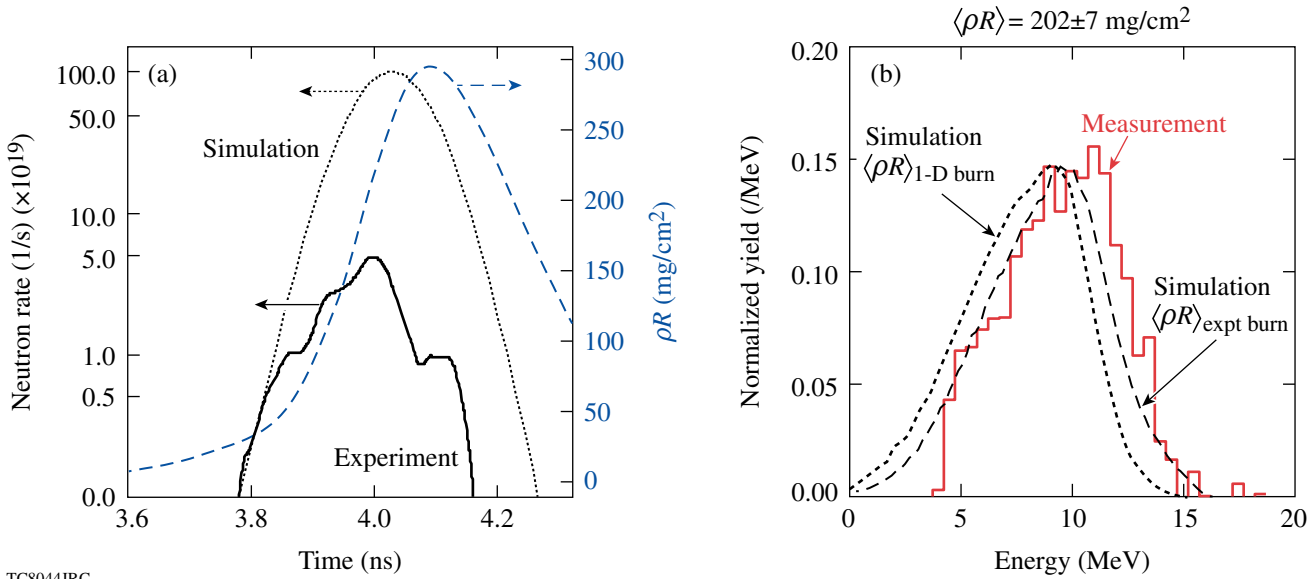

Figure 113.23

(a) The burn history measured (solid line) and predicted (dotted line). Also shown is the ρR evolution calculated with the 1-D code *LILAC* (dashed line, right axis). (b) Measured secondary-proton spectrum (solid line) for a 10-μm-thick CD shell with a 95-μm-thick D_2 cryogenic layer driven on an $\alpha = 2$ adiabat at $I = 5 \times 10^{14}$ W/cm^2. The dotted line shows the calculated spectrum averaged over the predicted 1-D burn, and the dashed line represents the calculated spectrum averaged over the experimental burn history.
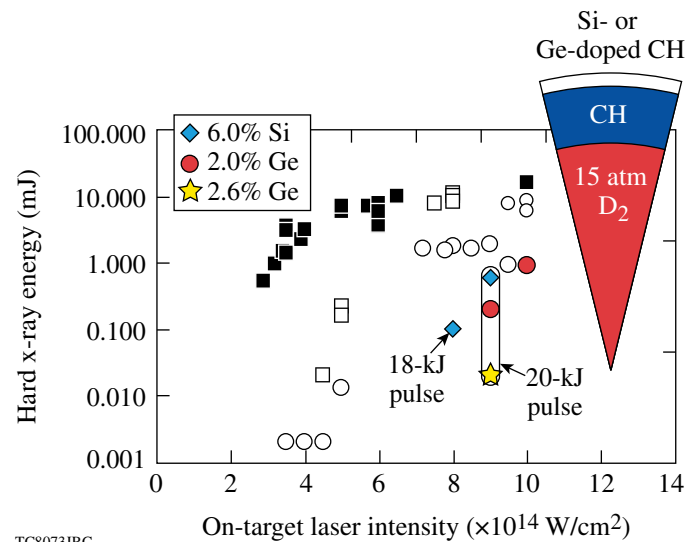

Figure 113.24

Measured bremsstrahlung radiation above 40 keV for the implosions with warm plastic (open circles), doped plastic (diamond, solid circle, and star), cryogenic 5-μm-thick CD (solid squares), and cryogenic 10-μm-thick CD (open squares) shells.

in pure-CH and CH shells doped with Si or Ge. The observed significant reduction in the signal level confirms the lower preheat level in the doped ablators. For comparison, Fig. 113.24 also shows the signal for cryogenic targets with 5- and 10-μm-thick CD shells.

In addition to the reduction in the hard x-ray signal, the shells with Si-doped layers show improved hydrodynamic stability. The radiation from the higher-Z dopant preheats the shell, reducing both the initial imprint levels[28,29] and the Rayleigh–Taylor instability growth. The improved stability of Si-doped shells with respect to the pure-CH shells results in an increase in both the experimental yields and the ratio of the experimental to the predicted yield. The latter is shown in Fig. 113.25. The increased yield is especially pronounced in the most-unstable, $\alpha = 2$ implosions when the thickness of the doped layer is 3 μm or greater. The stabilizing property of the high-Z dopants will be used in the future OMEGA cryogenic designs. Calculations show that the radiation from the dopant preferably preheats the higher-opacity CD layer without significantly heating the lower-opacity main fuel. This enhances cryogenic shell stability without compromising the fuel adiabat.
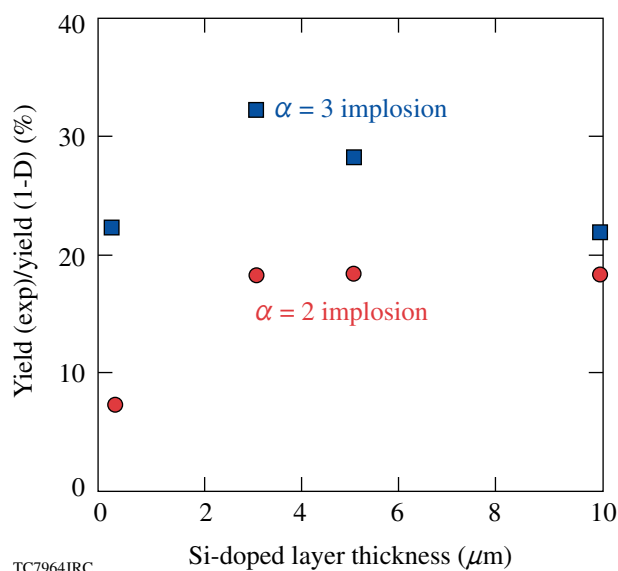

TC7964JRC

Figure 113.25
Ratio of the experimental yield and the predicted yield for warm-plastic-shell implosions with different Si-doped layer thicknesses.

Conclusions

Ignition target designs rely on low-adiabat, high-areal-density fuel compression. A series of implosions with 92- to 95-μm-thick cryogenic D_2 layers were performed on OMEGA to study the physics of ignition-relevant, low-adiabat fuel

assembly using the direct-drive configuration. The main sources of the adiabat degradation, observed in earlier experiments,[6,7] were attributed to (1) the shock mistiming resulting from inaccuracies in the laser-absorption modeling, (2) suprathermal-electron preheat generated by the two-plasmon-decay instability, and (3) under-sampling of higher ρR in the shell due to burn truncation. To increase the calculation accuracy, the nonlocal transport model was implemented in the 1-D hydrocode *LILAC*. High cryogenic areal density with $\langle \rho R \rangle > 200$ mg/cm^2 was measured in the experiments[11] when the shock timing was optimized using the nonlocal treatment of the heat transport and the suprathermal-electron-preheat source was mitigated.

REFERENCES

1. S. Atzeni and J. Meyer-ter-Vehn, *The Physics of Inertial Fusion: Beam Plasma Interaction, Hydrodynamics, Hot Dense Matter*, International Series of Monographs on Physics (Clarendon Press, Oxford, 2004).

2. J. D. Lindl, *Inertial Confinement Fusion: The Quest for Ignition and Energy Gain Using Indirect Drive* (Springer-Verlag, New York, 1998).

3. S. E. Bodner, D. G. Colombant, J. H. Gardner, R. H. Lehmberg, S. P. Obenschain, L. Phillips, A. J. Schmitt, J. D. Sethian, R. L. McCrory, W. Seka, C. P. Verdon, J. P. Knauer, B. B. Afeyan, and H. T. Powell, Phys. Plasmas **5**, 1901 (1998).

4. R. Betti and C. Zhou, Phys. Plasmas **12**, 110702 (2005).

5. T. R. Boehly, D. L. Brown, R. S. Craxton, R. L. Keck, J. P. Knauer, J. H. Kelly, T. J. Kessler, S. A. Kumpan, S. J. Loucks, S. A. Letzring, F. J. Marshall, R. L. McCrory, S. F. B. Morse, W. Seka, J. M. Soures, and C. P. Verdon, Opt. Commun. **133**, 495 (1997).

6. F. J. Marshall, R. S. Craxton, J. A. Delettrez, D. H. Edgell, L. M. Elasky, R. Epstein, V. Yu. Glebov, V. N. Goncharov, D. R. Harding, R. Janezic, R. L. Keck, J. D. Kilkenny, J. P. Knauer, S. J. Loucks, L. D. Lund, R. L. McCrory, P. W. McKenty, D. D. Meyerhofer, P. B. Radha, S. P. Regan, T. C. Sangster, W. Seka, V. A. Smalyuk, J. M. Soures, C. Stoeckl, S. Skupsky, J. A. Frenje, C. K. Li, R. D. Petrasso, and F. H. Séguin, Phys. Plasmas **12**, 056302 (2005).

7. T. C. Sangster, R. Betti, R. S. Craxton, J. A. Delettrez, D. H. Edgell, L. M. Elasky, V. Yu. Glebov, V. N. Goncharov, D. R. Harding, D. Jacobs-Perkins, R. Janezic, R. L. Keck, J. P. Knauer, S. J. Loucks, L. D. Lund, F. J. Marshall, R. L. McCrory, P. W. McKenty, D. D. Meyerhofer, P. B. Radha, S. P. Regan, W. Seka, W. T. Shmayda, S. Skupsky, V. A. Smalyuk, J. M. Soures, C. Stoeckl, B. Yaakobi, J. A. Frenje, C. K. Li, R. D. Petrasso, F. H. Séguin, J. D. Moody, J. A. Atherton, B. D. MacGowan, J. D. Kilkenny, T. P. Bernat, and D. S. Montgomery, Phys. Plasmas **14**, 058101 (2007).

8. F. H. Séguin, C. K. Li, J. A. Frenje, D. G. Hicks, K. M. Green, S. Kurebayashi, R. D. Petrasso, J. M. Soures, D. D. Meyerhofer, V. Yu. Glebov, P. B. Radha, C. Stoeckl, S. Roberts, C. Sorce, T. C. Sangster, M. D. Cable, K. Fletcher, and S. Padalino, Phys. Plasmas **9**, 2725 (2002).

9. J. Delettrez, R. Epstein, M. C. Richardson, P. A. Jaanimagi, and B. L. Henke, Phys. Rev. A **36**, 3926 (1987).

10. R. C. Malone, R. L. McCrory, and R. L. Morse, Phys. Rev. Lett. **34**, 721 (1975).

11. T. C. Sangster, V. N. Goncharov, P. B. Radha, V. A. Smalyuk, R. Betti, R. S. Craxton, J. A. Delettrez, D. H. Edgell, V. Yu. Glebov, D. R. Harding, D. Jacobs-Perkins, J. P. Knauer, F. J. Marshall, R. L. McCrory, P. W. McKenty, D. D. Meyerhofer, S. P. Regan, W. Seka, R. W. Short, S. Skupsky, J. M. Soures, C. Stoeckl, B. Yaakobi, D. Shvarts, J. A. Frenje, C. K. Li, R. D. Petrasso, and F. H. Séguin, "High-Areal-Density Fuel Assembly in Direct-Drive Cryogenic Implosions," submitted to Physical Review Letters.

12. V. N. Goncharov, J. P. Knauer, P. W. McKenty, P. B. Radha, T. C. Sangster, S. Skupsky, R. Betti, R. L. McCrory, and D. D. Meyerhofer, Phys. Plasmas **10**, 1906 (2003).

13. K. Anderson and R. Betti, Phys. Plasmas **11**, 5 (2004).

14. S. Chandrasekhar, in *Hydrodynamic and Hydromagnetic Stability*, International Series of Monographs on Physics (Clarendon Press, Oxford, 1961), p. 428.

15. W. L. Kruer, *The Physics of Laser–Plasma Interactions*, Frontiers in Physics, Vol. 73, edited by D. Pines (Addison-Wesley, Redwood City, CA, 1988), Chap. 4, p. 39.

16. I. V. Igumenshchev, V. N. Goncharov, W. Seka, D. Edgell, and T. R. Boehly, Phys. Plasmas **14**, 092701 (2007).

17. L. Spitzer, Jr. and R. Härm, Phys. Rev. **89**, 977 (1953).

18. A. Sunahara, J. A. Delettrez, C. Stoeckl, R. W. Short, and S. Skupsky, Phys. Rev. Lett. **91**, 095003 (2003).

19. V. N. Goncharov, O. V. Gotchev, E. Vianello, T. R. Boehly, J. P. Knauer, P. W. McKenty, P. B. Radha, S. P. Regan, T. C. Sangster, S. Skupsky, V. A. Smalyuk, R. Betti, R. L. McCrory, D. D. Meyerhofer, and C. Cherfils-Clérouin, Phys. Plasmas **13**, 012702 (2006).

20. N. A. Krall and A. W. Trivelpiece, *Principles of Plasma Physics* (San Francisco Press, Inc., San Francisco, 1986), p. 316.

21. A. V. Maksimov, V. P. Silin, and M. V. Chegotov, Sov. J. Plasma Phys. **16**, 331 (1990).

22. V. N. Goncharov and G. Li, Phys. Plasmas **11**, 5680 (2004).

23. W. Seka, D. H. Edgell, J. P. Knauer, J. F. Myatt, A. V. Maximov, R. W. Short, T. C. Sangster, R. E. Bahr, R. S. Craxton, J. A. Delettrez, V. N. Goncharov, I. V. Igumenshchev, and D. Shvarts, "Time-Resolved Absorption in Cryogenic and Room-Temperature, Direct-Drive Implosions," submitted to Phys. Plasmas (invited).

24. A. Simon, R. W. Short, E. A. Williams, and T. Dewandre, Phys. Fluids **26**, 3107 (1983).

25. C. Stoeckl, V. Yu. Glebov, D. D. Meyerhofer, W. Seka, B. Yaakobi, R. P. J. Town, and J. D. Zuegel, Rev. Sci. Instrum. **72**, 1197 (2001).

26. V. A. Smalyuk, D. Shvarts, R. Betti, J. A. Delettrez, D. H. Edgell, V. Yu. Glebov, V. N. Goncharov, R. L. McCrory, D. D. Meyerhofer, P. B. Radha, S. P. Regan, T. C. Sangster, W. Seka, S. Skupsky, C. Stoeckl, B. Yaakobi, J. A. Frenje, C. K. Li, R. D. Petrasso, and F. H. Séguin, "The Role of Hot-Electron Preheat in the Compression of Direct-Drive Imploding Targets with Cryogenic D_2 Ablators," submitted to Physical Review Letters.

27. P. B. Radha, V. N. Goncharov, T. J. B. Collins, J. A. Delettrez, Y. Elbaz, V. Yu. Glebov, R. L. Keck, D. E. Keller, J. P. Knauer, J. A. Marozas, F. J. Marshall, P. W. McKenty, D. D. Meyerhofer, S. P. Regan, T. C. Sangster, D. Shvarts, S. Skupsky, Y. Srebro, R. P. J. Town, and C. Stoeckl, Phys. Plasmas **12**, 032702 (2005).

28. M. Karasik *et al.*, Bull. Am. Phys. Soc. **49**, 276 (2004).

29. A. N. Mostovych, D. G. Colombant, M. Karasik, J. P. Knauer, A. J. Schmitt, and J. L. Weaver, "Enhanced Direct-Drive Implosion with Thin High-*Z* Ablation Layers," to be published in Physical Review Letters.